JOURNAL OF SYNCHROTRON RADIATION

ISSN 1600-5775

Received 22 October 2014
Accepted 18 February 2015

Edited by A. F. Craievich, University of São Paulo, Brazil

Keywords: instrumentation; *in situ* XAS; DXAS; platinum; nanoparticles; synthesis.

Supporting information: this article has supporting information at journals.iucr.org/s

A dispenser–reactor apparatus applied for *in situ* XAS monitoring of Pt nanoparticle formation

Jocenir Boita,[a] Marcus Vinicius Castegnaro,[a] Maria do Carmo Martins Alves[b] and Jonder Morais[a]*

[a]Laboratório de Espectroscopia de Elétrons (LEe-), Instituto de Física, Universidade Federal do Rio Grande do Sul (UFRGS), Av. Bento Gonçalves 9500, CEP-91501-970, Porto Alegre, Rio Grande do Sul – RS 15051, Brazil, and [b]Instituto de Química, Universidde Federal do Rio Grande do Sul (UFRGS), Av. Bento Gaonçalves 9500, CEP-91501-970, Porto Alegre, Rio Grande do Sul – RS 15003, Brazil. *Correspondence e-mail: jonder@if.ufrgs.br

In situ time-resolved X-ray absorption spectroscopy (XAS) measurements collected at the Pt L_3-edge during the synthesis of Pt nanoparticles (NPs) in aqueous solution are reported. A specially designed dispenser–reactor apparatus allowed for monitoring changes in the XAS spectra from the earliest moments of Pt ions in solution until the formation of metallic nanoparticles with a mean diameter of 4.9 ± 1.1 nm. By monitoring the changes in the local chemical environment of the Pt atoms in real time, it was possible to observe that the NPs formation kinetics involved two stages: a reduction-nucleation burst followed by a slow growth and stabilization of NPs. Subsequently, the synthesized Pt NPs were supported on activated carbon and characterized by synchrotron-radiation-excited X-ray photoelectron spectroscopy (XPS), X-ray diffraction (XRD) and extended X-ray absorption fine structure (EXAFS). The supported Pt NPs remained in the metallic chemical state and with a reduced size, presenting slight lattice parameter contraction in comparison with the bulk Pt values.

1. Introduction

Optimized control of the electronic and structural properties of nanomaterials is determinant for tailoring their final application. A wide range of experimental techniques have been applied for this task; in particular, X-ray absorption spectroscopy (XAS) is one of the most powerful tools used to investigate advanced materials on the atomic level. For this purpose, *in situ* dispersive X-ray absorption spectroscopy (DXAS) measurements allow time-resolved structural and electronic information to be obtained under operando conditions, since these experiments can be carried out over a wide range of temperatures, pressures and environments (Bordiga *et al.*, 2013).

Considering the area of catalysis, *in situ* DXAS measurements have proven to be very efficient for monitoring and understanding many chemical reactions (Boita *et al.*, 2014*a*,*b*; Erickson *et al.*, 2011; Bernardi *et al.*, 2010, 2011; Hannemann *et al.*, 2007; Girardon *et al.*, 2005; Guilera *et al.*, 2009; Odzak *et al.*, 2001). In recent years, our group has performed XAS and DXAS experiments on advanced catalysts during processes under specific atmospheres. Recently, this technique was used to investigate the behaviour of Pt_xPd_{1-x} nanoparticles (NPs) during reduction and sulfidation processes (Bernardi *et al.*, 2011), and enabled us to follow changes in the atomic arrangement and chemical environment of Pt and Pd atoms during these processes. In a recent work (Boita *et al.*, 2014*a*),

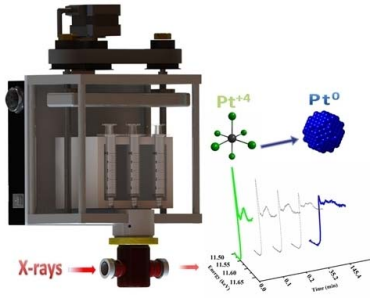

time-resolved XAS was applied to investigate the sulfidation process in $Pt_{0.3}Pd_{0.7}$ NPs and its reversibility by a reduction process.

It is known that the full potentialities of an experimental technique applied to any research problem depend on the availability of proper instrumentation. For XAS measurements of solid samples, many reactors, or reaction cells, have been developed in order to make *in situ* measurements possible. Erickson and co-workers. (Erickson *et al.*, 2011), for example, developed an electrochemical cell for *in situ* XAS studies, which allows a high flow of oxygen to the working electrode through a window of poly(dimethylsiloxane), allowing XAS studies during oxygen reduction eletrocatalysis. Hannemann and collaborators (Hannemann *et al.*, 2007) developed a reactor for XAS (in fluorescence mode) and transmission X-ray diffraction analysis during catalytic processes. Their design allowed structural studies during the reduction of metallic particles supported on Al_2O_3 and CeO_2. Many other experimental apparatus for XAS measurements of solid samples may be found in the literature (Bernardi *et al.*, 2007; Watanabe *et al.*, 2007), but reaction cells for liquids are scarce. In this case, it is common to place the liquid sample in homemade cells closed with Kapton® films. Sarma *et al.* (2007), for example, used a PTFE cell for their XAS measurements during the formation of Pt–Ru NPs in ethylene glycol. They collected aliquots of the solution at different stages of the synthesis that were then placed in the XAS cell.

To enable acquiring time-resolved XAS data during reactions in liquid media, we recently developed a reaction cell which was employed for studying the formation of copper compounds by *in situ* DXAS (Boita *et al.*, 2014*b*). To perform the present work, this cell was attached to a homemade liquid dispenser, which allows remote control of the dosing speed of solutions into the reaction cell. In this paper, we describe the complete experimental apparatus that allowed the acquisition of time-resolved DXAS data during the entire reactive process in the liquid phase. It can be used to study a wide range of reactions, although here we focused on monitoring the kinetics of platinum nanoparticle formation in an aqueous solution. Recently (Boita *et al.*, 2014*c*), we employed the instrumentation discussed here to study the formation mechanism of small platinum nanoparticles obtained by the polyol method in ethylene glycol.

Pt NPs have a wide range of applications (Zhang *et al.*, 2013; Ramalingam *et al.*, 2013; Steinfeldt, 2012; Harada & Kamigaito, 2011; Scheeren *et al.*, 2003), and many methods to synthesize them have been developed; for example, using sputtering (Ramalingam *et al.*, 2013), synthesis in ionic liquids (Scheeren *et al.*, 2003) and polyol synthesis (Kim *et al.*, 2006), among others. The synthesis presented here is a variation of that employed in a previous work for obtaining Pd NPs (Castegnaro *et al.*, 2013) using an eco-friendly wet chemical route based on the reduction of a metal salt by ascorbic acid. Therefore, we report here on time-resolved DXAS analysis during the formation of Pt NPs as well as the *ex situ* characterization results by transmission electron microscopy (TEM), high-resolution transmission electron microscopy (HRTEM), X-ray photoelectron spectroscopy (XPS), X-ray diffraction (XRD), and extended X-ray absorption fine structure (EXAFS) of the as-prepared and carbon-supported Pt NPs (Pt/C).

2. Experimental methods

2.1. Experimental setup for *in situ* XAS

In order to follow the evolution of the Pt atomic environment during the formation of Pt NPs in solution, a dispenser–reactor apparatus was designed and built (Fig. 1). A liquid dispenser allowed us to remotely control the dosing speed of solutions into the attached reaction cell. This dispenser was designed to adjust the flow velocity of the reagents by controlling the speed of a stepper motor. As shown in Fig. 1, two linear spindles are triggered by the motor to push the pistons of the syringes, injecting the solution into the reaction cell. The dispenser is basically composed of the following parts, which are indexed in Fig. 1: a stepper motor with a step size of 3 mm (I), which enables the clockwise and counterclockwise movement of the pulley system (II), which is composed of two belt pulleys (step size 3 mm) coupled to a pair of spindles. The spindles move an aluminium rod vertically, with the goal of pushing the syringe system (III), and inject the liquid into the reaction cell (VI) at a finely tuned rate. This rate was remotely controlled by the electronics coupled to the system (IV), which allowed the liquid dispensing rate to be adjusted between 0.06 ml s^{-1} and 0.48 ml s^{-1}, using three syringes with a volume of 5 ml. For applications which require different dosing speeds, in addition to the stepper motor speed adjustment, it is also possible to change the number and/or the volume capacities of the syringes used for adding the reactants, adjusting the dosing flow. Never-

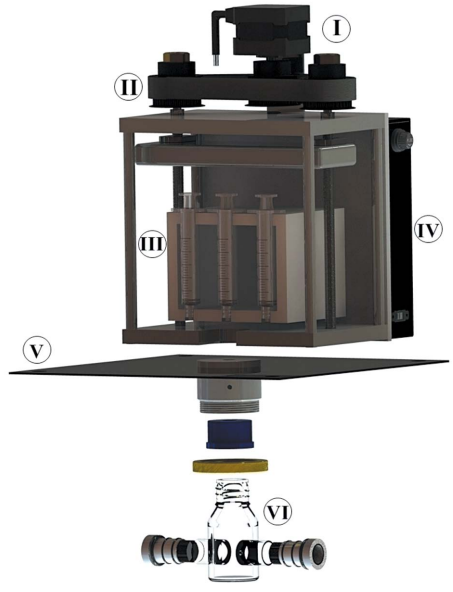

Figure 1
Apparatus used during the *in situ* DXAS experiments. The indexed parts are: stepper motor (I), pulley system (II), syringe system (III), electronic circuits (IV), supporting plate (V) and reaction cell (VI).

theless, prior to the synchrotron experiments, it is mandatory to perform several syntheses with the apparatus in order to find the correct dosing speed that provides the desired nanoparticles size distribution. The reaction cell has been described in a recent work (Boita *et al.*, 2014*b*). The whole system is attached to a metallic plate (V), which can be coupled to the three-axis motorized stage of the beamline end-station, making it easy to align the reactor windows with the synchrotron X-ray beam path.

In this paper, we applied the proposed apparatus to follow DXAS measurements at the Pt L_3-edge during the formation of Pt NPs in aqueous solution. Details of the chemical reaction are presented below.

2.2. Nanoparticle synthesis

The synthesis employed to obtain platinum NPs consisted of a wet chemical reduction method at room temperature that used eco-friendly stabilizing and reducing agents, namely sodium citrate and ascorbic acid, respectively. Recently, we have successfully obtained Pd nanoworms using this same method (Castegnaro *et al.*, 2013). Here, our main goal was to follow the kinetics of Pt NP formation by observing the changes in the vicinities of the Pt atoms in the solution.

The *in situ* dispersive XAS study was carried out using the experimental setup described in the previous section. The synthesis reaction was carried out at room temperature and under constant stirring, and all the solutions employed deionized water as the solvent. Initially, a 0.02 mmol solution of K_2PtCl_6 (Vetec) and a 0.15 mmol solution of sodium citrate (Sigma-Aldrich) were mixed in the reaction cell. The volume of this starting solution was sufficient to completely cover the Kapton® windows of the reaction cell. After 10 min under constant stirring, the addition of the reducing agent was initiated, *i.e.* an aqueous solution containing 3 mmol of ascorbic acid (Vetec) was added at a dosing rate of 0.38 ml s^{-1} in 22 s. The total reaction solution in the cell was 20 ml. The dosing speed and time, as well as the molarity and volume of the solutions of each reactant, were previously determined in our laboratory for achieving monodisperse Pt NPs. After 150 min of reaction, the final colloidal solution was adsorbed on activated carbon (Pt/C), using the method previously described (Castegnaro *et al.*, 2013) for obtaining a noble metal-based heterogeneous catalyst.

2.3. *In situ* DXAS measurements

In situ DXAS experiments aim to monitor the Pt L_3-edge (11564 eV) during the formation of Pt NPs. These measurements were performed at the DXAS beamline at the LNLS (Brazilian Synchrotron Light Laboratory) (Cezar *et al.*, 2010). The LNLS storage ring operates at 1.37 GeV with a maximum fill current of 250 mA. The beamline monochromator consists of a curved Si(111) crystal (dispersive polychromator) that focuses the beam on the horizontal plane to about 150 µm. A vertical focusing to about 200 µm is provided by a Rh-coated mirror. The incident X-ray beam flux at the sample position was 2×10^{11} photons mm^{-2} s^{-1} at 14 keV and 100 mA stored beam current. The beamline energy resolution at the Pt L_3-edge was 2.9 eV. The reaction cell was installed at the beamline, taking care to place it at the X-ray beam focal point. The time-resolved spectra were collected by a position-sensitive CCD camera. The acquisition time of each spectrum was 6.3 s.

2.4. *Ex situ* measurements

Transmission electron micrographs of the as-prepared Pt NPs were obtained using a Jeol JEM-1200 EX II working at an accelerating voltage of 100 kV. For this, a drop of the colloidal solution was placed on a Formvar-coated copper grid (300 mesh, TED PELLA) and dried at room temperature in a desiccator. About 850 NPs from different parts of the image were taken into account (Image J 1.45) in order to estimate the size distribution of the NPs, which were fitted (*OriginPro 8*) considering a Gaussian–Lorentzian sum function. The high-resolution TEM (HRTEM) analysis was performed in a Jeol JEM-3010 URP microscope at LNNano (Brazilian Nanotechnology National Laboratory) working at 300 kV. The sample was prepared by placing a drop of the as-prepared colloid on a copper grid coated with an ultrathin carbon film supported by a lacey carbon film (400 mesh, TED PELLA).

The carbon-supported Pt NPs (Pt/C) were later analyzed at the SXS beamline (Tolentino *et al.*, 1998) at LNLS for synchrotron-excited XPS measurements. The use of synchrotron radiation provided spectra with an intense signal and an excellent overall energy resolution. The spectra were collected using an InSb(111) double-crystal monochromator at fixed photon energy of 1840 eV. The hemispherical electron analyzer (SPECS Phoibos 150) was set at a pass energy of 30 eV and the energy step was 0.1 eV, with an acquisition time of 500 ms per point. The energy calibration of the analyzer was performed using a standard Au foil [Au $4f_{7/2}$ peak at 84 eV (Moulder *et al.*, 1992)]. The C 1*s* peak [284.5 eV (Moulder *et al.*, 1992)] was considered as an internal reference in order to verify possible charging effects. The accuracy of the experimental binding energy values was ±0.1 eV. The sample was placed on carbon tape and the XPS spectra were collected at a 45° take-off angle, at room temperature. The base pressure inside the analysis chamber was about 8×10^{-10} mbar. *XPS Peak* (version 4.1) was used to fit the XPS data. All peaks were adjusted using a Shirley-type background (Seah & Brown, 1999) and an asymmetric Gaussian–Lorentzian sum function (20% Lorentzian contribution).

The XRD measurements were performed on Pt/C samples using a Siemens D500 with Cu K_α radiation (17.5 mA, 40 kV and λ = 1.54 Å). The step size was 0.05° and the acquisition time was 1 s per point, ranging from 20° to 90°. The diffraction peaks were indexed using the Crystallographica Search-Match (version 2.1.1.1) and ICSD database (ICSD number 64917). The *FULLPROF* package (version 5.20) was used for structure profile refinement by the Rietveld method, using a modified pseudo-Voigt function (Finger *et al.*, 1994) for peak fitting and CIF number 64917 as the reference. Using the peak positions and full width at half-maximum (FWHM) obtained from the Rietveld refinement, Scherrer's equation was applied

(supposing spherical crystallites) to estimate the crystallite mean size from the XRD pattern.

The steady-mode XAS experiments were performed on the Pt/C sample using the XAFS1 beamline of the LNLS (Tolentino *et al.*, 2001). The XAS spectra were collected at the Pt L_3-edge using a channel-cut Si(111) crystal and three argon-filled ionization chambers. A standard Pt foil was used for energy calibration. Four scans were collected in order to improve the signal-to-noise ratio. Each spectrum was acquired in the range 11440–12200 eV with a 2 eV step and 2 s per point.

2.5. XANES and EXAFS data analysis

The time-resolved DXAS data acquired during the reaction were analyzed to extract the kinetics of the Pt^0 fraction during the formation of Pt NPs. The initial XANES curve of the reaction and that of the Pt/C powder were chosen as reference curves of the Pt^{4+} and Pt^0 chemical states, respectively, and used to evaluate the temporal evolution of the XANES spectra. The following equation was used for the linear combination: $\mu_{obs} = C_1\mu^{4+} + C_2\mu^0$, where μ_{obs} is the observed absorption coefficient, while μ^0 and μ^{4+} are the two representative XANES curves of Pt^0 (Pt/C powder) and Pt^{4+} (first spectrum collected), respectively. The corresponding coefficients were normalized ($C_1 + C_2 = 1$) in order to quantify the relative fraction of each chemical species. The *ATHENA* (Ravel & Newville, 2005) program was used for the linear combination procedures.

The *in situ* XAS spectra were analyzed in accordance with the standard procedure of data reduction (Koningsberger & Prins, 1988), using the *IFEFFIT* package (Newville, 2001). The *FEFF8* code was used to obtain the phase shift and scattering amplitudes (Zabinsky *et al.*, 1995), considering a Pt face-centred-cubic (lattice parameter a = 3.911 Å) cluster with a radius of 10 Å. The EXAFS signal $\chi(k)$ was extracted and then Fourier transformed (FT) using a Kaiser–Bessel window with a Δk range of 8.0 Å for the Pt L_3-edge. The $\chi(k)$ data were k^2-weighted to compensate for the damping of EXAFS oscillations in the high-k region. During the EXAFS fitting, the number of free parameters (used as variables in the fitting procedure) was always lower than the number of independent points in the fitted region. The amplitude reduction term (S_0^2) value was fixed at 0.86, which was obtained from the fitting of standard Pt foil.

3. Results and discussion

3.1. *In situ* DXAS

The reduction of K_2PtCl_6 by ascorbic acid during the formation of Pt NPs at room temperature was monitored by time-resolved DXAS. Prior to the main experiment, we collected the XANES spectra of the reference aqueous solutions, namely K_2PtCl_6 and the mixture of K_2PtCl_6 and sodium citrate (SC). Note that the K_2PtCl_6 + SC mixture was the starting solution for the reaction. The spectra are shown in Fig. 2, along with the spectra of standard PtO_2 and Pt foil. The

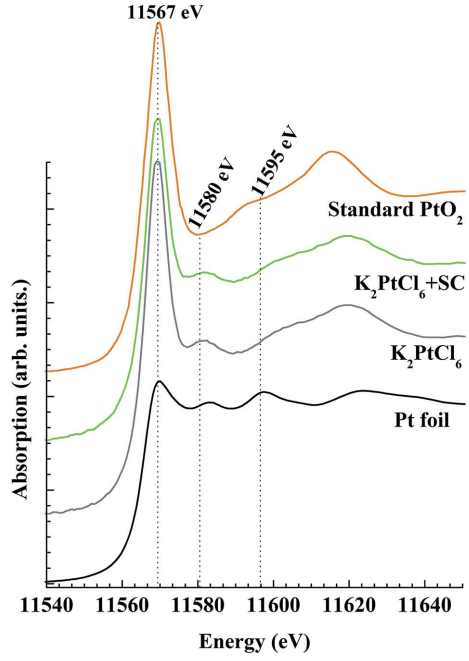

Figure 2
Pt L_3-edge XANES spectra obtained for reference solutions (K_2PtCl_6, and K_2PtCl_6 + SC), standard PtO_2 and Pt foil.

XANES spectra in Fig. 2 were normalized and displaced vertically for ease of comparison.

The XANES curve acquired for the reference solution K_2PtCl_6 showed the typical features of Pt^{4+} in an octahedral geometry (Ankudinov *et al.*, 2000; Boita *et al.*, 2014*c*). Additionally, it has been reported that the peak at 11580 eV occurs due to final state effects that take place in hybridized *d* orbitals originating from the Pt–Cl interaction (Sham, 1986). The spectrum of the starting solution (K_2PtCl_6 + SC) presents the same features, implying that the addition of SC did not change the chemical state and environment of the absorber atom. We have not observed changes in the XANES spectra due to exposition to photons from the beamline, and therefore no indication of NP formation induced by X-ray radiolysis.

Fig. 3 shows the time-resolved XANES data collected during the formation of Pt NPs in solution. One may observe how three prominent features (*A*, *B* and *C* at 11567 eV, 11580 eV and 11595 eV, respectively) evolve during the reaction. The reaction was initiated by the addition of ascorbic acid (0 min of reaction) solution into the starting solution by the dispenser. As can be inferred from the decrease in the intensity of the white line, the reduction of the Pt^{4+} species was a quick process. During the first 12.6 s after initiating ascorbic acid solution dosing, the most significant changes in the Pt L_3-edge XANES were noticeable.

Initially, a clear decrease in the intensity of the white line (feature *A*) could be observed; this effect is due to the occupation of the existing holes in the 5*d* band, and it indicates a reduction in the oxidation state of the absorber atoms. In fact, it is expected that, at a lower intensity of the white line, the electron occupancy of the valence orbitals is higher and the oxidation state of the Pt absorber is lower (Sham, 1986;

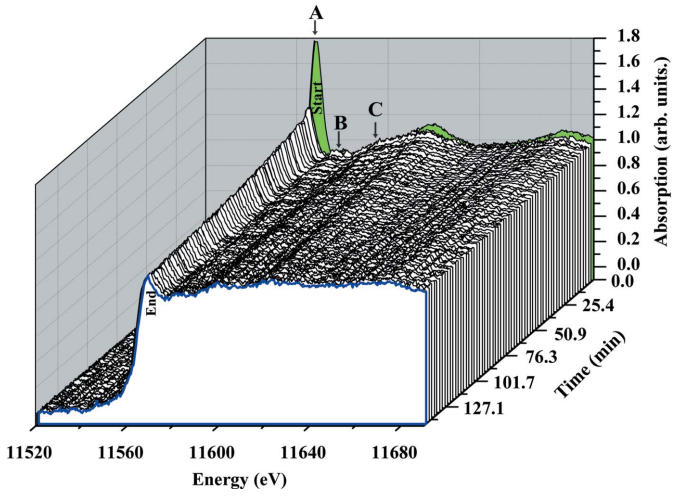

Figure 3
Evolution of the XANES region during Pt NP formation. The overall reaction was monitored for 145.4 min. The accumulation time for each spectrum was 6.3 s during the first 4.3 min of reaction. After this time, one spectrum was collected every 31.5 s to improve the signal-to-noise ratio.

Ankudinov *et al.*, 2000). Additionally, a new peak appeared, feature *C*, which is a characteristic of metallic platinum (Ankudinov *et al.*, 2000; Bernardi *et al.*, 2010). As the reaction evolved, the general shape of the XANES spectrum became more akin to the standard Pt foil, but with a remarkable damping of the oscillations. This damping may be due to thermal and structural disorder, or it may be an effect of reducing the coordination number of Pt in the nano-sized particles (Frenkel *et al.*, 2001; Frenkel, 2012).

The changes in the Pt L_3-edge XANES region during the reaction can be better observed in Fig. 4(*a*), where 30 spectra have been selected (see also Fig. S2 in the supporting information). Additionally, Fig. 4(*b*) shows a comparison between the data acquired just before the addition of ascorbic acid (0 min of reaction), the spectrum collected at the end of the reaction (145.4 min), the XANES of carbon-supported Pt NPs (Pt/C) and the XANES of the reference Pt foil. It is clear that the latter three spectra are very similar, indicating that the reduction process was achieved and thereby the synthesis led to Pt^0 NPs. Moreover, we also concluded from these XANES signals that the process of adsorption on activated carbon did not change the oxidation state of the Pt absorber atoms, and thus metallic Pt NPs are available for catalytic processes in the Pt/C powder.

A typical linear combination of a XANES spectrum that yielded the relative fraction of Pt^{4+} (green curve) and Pt^0 in Pt/C powder (blue curve) is shown in Fig. 5(*a*) for the spectrum (open circles) collected after 6.3 s of the reaction. The fractions of metallic platinum (C_2 values) obtained from the linear combination of several XANES curves collected during the *in situ* measurement are shown in Fig. 5(*b*). Each point corresponds to the linear combination of a selected XANES spectrum.

As qualitatively predicted by the time-resolved curves in Fig. 3, Fig. 5(*b*) indicates that the reduction of Pt^{4+} to Pt^0 is a

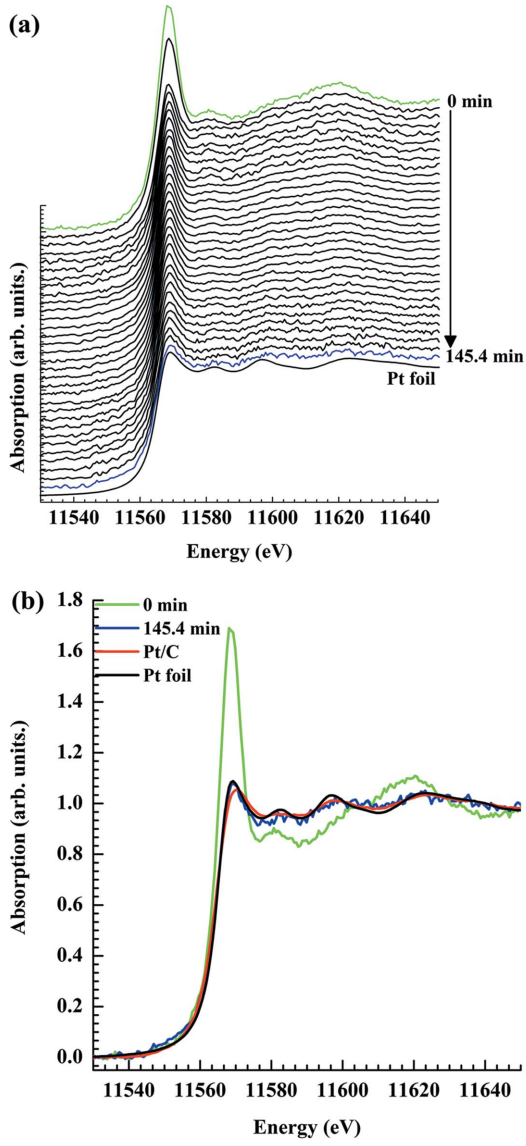

Figure 4
(*a*) Representative XANES curves revealing the changes during the formation of Pt NPs. (*b*) Comparison between the Pt foil XANES, the first (0 min) and the last (145.4 min) spectra collected during the reaction, and the spectrum of carbon-supported Pt NPs (Pt/C).

fast process that takes place mostly during the first seconds of the reaction. In fact, after about 100 s, the Pt^0 contribution in the XANES spectrum was almost 70%. At 300 s, the Pt^0 fraction was about 80%. After that, the amount of metallic platinum slowly went up to almost 100%. Therefore, it was possible to observe two distinct stages during the time evolution of the reaction in Fig. 5(*b*). The first corresponds to the nucleation. The sudden increase in $\%Pt^0$ can be interpreted as the transition from early nuclei to small nanoparticles. This is a typical behaviour of a fast and limited nucleation process, ignited by the reduction of the salt precursor by ascorbic acid, which is in accordance with LaMer's nucleation burst scenario (LaMer & Dinegar, 1950). In this case, the high rate of nucleation leads to the burst of nuclei formation in a short period of time, and consequently

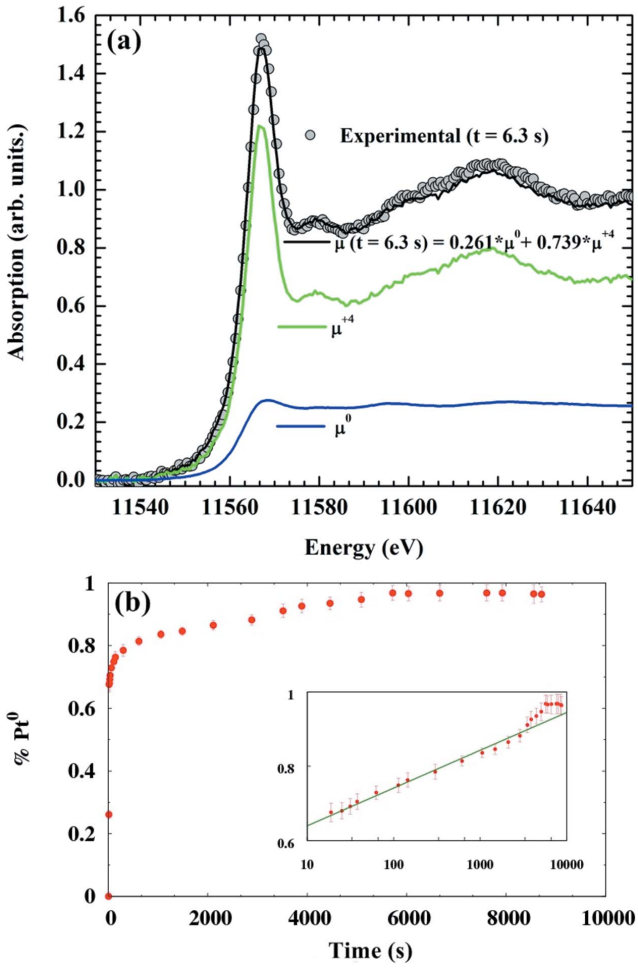

Figure 5
Linear combination of time-resolved XANES data: (*a*) linear combination of the curve measured at t = 6.3 s using a linear combination of Pt^{4+} (μ^{4+}) and Pt^0 (μ^0) XANES spectra. (*b*) The resulting temporal evolution of the Pt_0 fraction during Pt NP synthesis. The inset shows the same curve plotted on linear–log scale, and the solid line corresponds to the best algebraic fit to 0.538 (1) + 0.044 (2) log(t).

rapidly lowers the metal ion concentration to below that required to allow further nucleation. This process ensures the formation of approximately homogeneous size NPs after the stabilization of the reaction (Sugimoto, 1987; Viswanatha & Sarma, 2007). A similar behaviour has been observed during the polyol synthesis of Pt NPs (Boita *et al.*, 2014*c*). The second stage is much slower, corresponding to the stabilization of the kinetics of Pt NP formation. This stage, presenting a logarithmic dependence with time, would occur when the SC acts as both passivating and capping agent, adsorbed onto the NP surface. The SC eventually completely halts NP growth and prevents agglomeration by steric repulsion between the adsorbed layers (Boönnemann & Nagabhushana, 2008).

Thus, the experimental apparatus proposed here proved to be useful for monitoring the formation of Pt NPs *via* the reduction of K_2PtCl_6 by ascorbic acid assisted by citric acid. It allowed detailed information to be acquired on the synthesis kinetics, and hence it could also be useful to better understand reactions in liquid media by *in situ* XAS measurements.

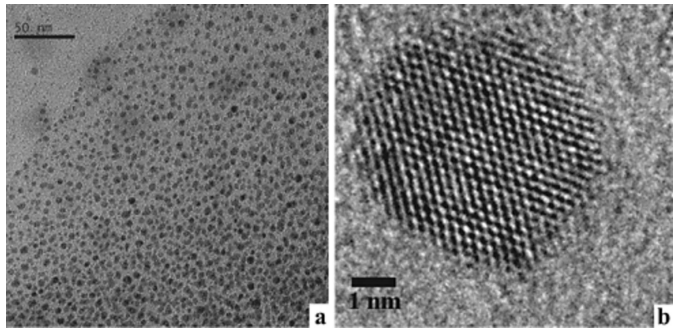

Figure 6
Representative TEM micrograph of Pt NPs (*a*) and HRTEM image of a single Pt NP (*b*).

3.2. TEM and HRTEM results

During the TEM analysis, several parts of the grid showed Pt NPs with a quasi-spherical shape and mean diameter of 4.9 ± 1.1 nm (the histogram of the diameter distribution is shown in Fig. S1 in the supporting information), as can be seen in Fig. 6(*a*). At the highest magnification and at high resolution (Fig. 6*b*), the crystallinity of the Pt NPs was confirmed. The particle in Fig. 6(*b*) has a diameter of about 5 nm.

3.3. XPS, XRD and EXAFS results

XPS, XRD and XAS measurements were also performed after the adsorption of the colloid on activated carbon in order to probe the structural and electronic properties of the resulting Pt/C sample, a material that is relevant for several catalytic processes.

The Pt 4*f* region of the synchrotron-excited photoemission spectrum of the carbon-supported Pt NPs is shown in Fig. 7. It presents two asymmetrical peaks (Pt $4f_{7/2}$ and Pt $4f_{5/2}$) that were deconvoluted in two chemical components. The lower

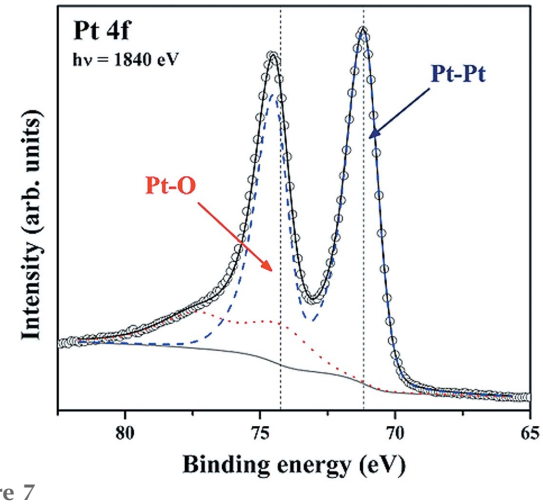

Figure 7
Pt 4*f* region of the XPS spectra of carbon-supported Pt NPs. The open circles indicate the raw data and the overlying continuous black line represents the sum of the components (coloured dashed lines) used in the fitting. The continuous grey line represents the Shirley-type background. The vertical lines indicate the binding energies of the observed chemical components.

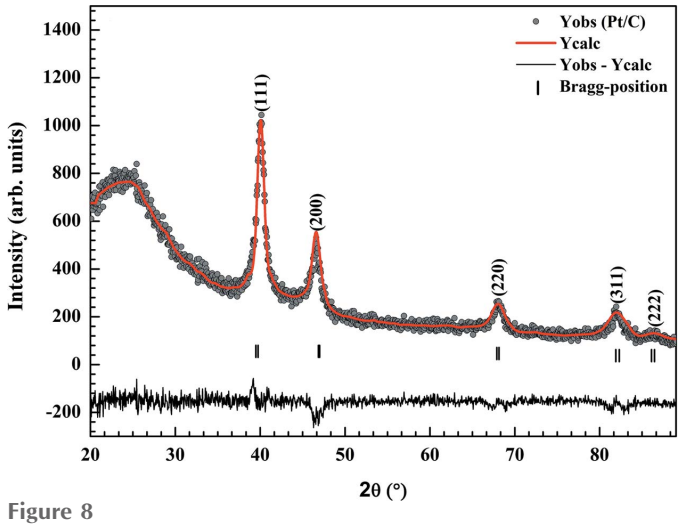

Figure 8
X-ray diffraction pattern (Yobs, grey circles) of the carbon-supported Pt NPs and the simulated curve by applying the Rietveld refinement (Ycalc, red line).

binding energy one (71.2 eV) is related to Pt–Pt bonds in Pt^0. These binding energy values and the spin–orbit splitting (3.3 eV) are in agreement with the literature for metallic platinum (Moulder *et al.*, 1992; Scheeren *et al.*, 2003; Aricò *et al.*, 2001; Mandal *et al.*, 2004). The component at 74.3 eV (red dashed line in Fig. 7) corresponds to Pt–O bonds (Moulder *et al.*, 1992; Scheeren *et al.*, 2003; Aricò *et al.*, 2001).

The ratio between the Pt–Pt and Pt–O peak areas is about 6:1. This result implies that the NPs anchored at the surface of the Pt/C sample have Pt atoms mostly in the metallic chemical state and that the oxide component was due to exposure to air.

The crystal structure of carbon-supported Pt NPs was probed by XRD. The full-scale pattern obtained (Yobs) is shown in Fig. 8, where one can see the five characteristic diffraction peaks of metallic platinum in the face-centred-cubic phase. In Fig. 8, the simulated curve (Ycalc) is also shown, which was obtained by applying the Rietveld method with the *FULLPROF* code. The difference curve (Yobs − Ycalc) reflects the low χ^2 of the refinement (1.57).

The results of the structure profile refinement are summarized in Table S1 in the supporting information, where the structural parameters of ICSD number 64917 are also presented for comparison. A remarkable feature observable in the Pt/C XRD data is the broadening of the Bragg peaks, which is an effect of the reduced crystallite size (Scheeren *et al.*, 2003). In the same table, the average sizes of Pt crystallites (D) are presented, as estimated by applying Scherrer's equation (supposing spherical crystallites) for the diffraction peaks related to the (111), (200), (220), (311) and (222) crystal planes of face-centred-cubic Pt. By averaging the values of D for each plane, an average size of about 6.6 ± 2.1 nm was estimated for the Pt crystallites. As pointed out previously, the value obtained by TEM analysis was 4.9 ± 1.1 nm.

As shown in Table S1, the Bragg positions are in agreement with the values found in the database, assigned for bulk Pt. By comparing the d_{hkl} values found for Pt NPs and for bulk Pt from the database, one can note that the interplanar distances in the Pt NPs are contracted, *i.e.* this implies that the Pt lattice parameter observed in Pt/C is smaller than that for bulk Pt. The reduction of the lattice parameter with a decrease in the particle size of metallic NPs has been reported in many experimental and theoretical papers (Lamber *et al.*, 1995; Qi, 2006). By calculating the Pt lattice parameter (a) using the interplanar distances of each crystal plane and averaging the obtained values, it can be found that a assumes a mean value of 3.895 Å. In the database, we found an a value of 3.911 Å. Thereby, we observed a relative contraction of 0.35% in the Pt lattice parameter. This is not a conclusive result, since it is within the experimental error, but it can be considered as an indication of Pt unit-cell contraction in the Pt/C sample.

Ex situ XAS measurements at the Pt L_3-edge were performed in order to extract the EXAFS signal, and then to obtain the structural parameters of the Pt/C sample by probing the short-range order around the Pt atoms within the NPs. Fig. 9 shows the EXAFS $\chi(k)$ signals (a) and the corresponding Fourier transforms (FT) (b) obtained for the as-prepared Pt/C and for a standard Pt^0 foil. The best-fit results are also presented in Fig. 9. The EXAFS signal of Pt/C NPs displays smothered oscillations, as expected due to the short-range order of the NPs. A minimum in the backscattering amplitude of heavier scatterers produces a double peak in the FT (Ramsauer Townsend effect), which in fact corresponds to the coordination shell of Pt. The changes in the EXAFS signal at the low-R region for the carbon-supported sample corre-

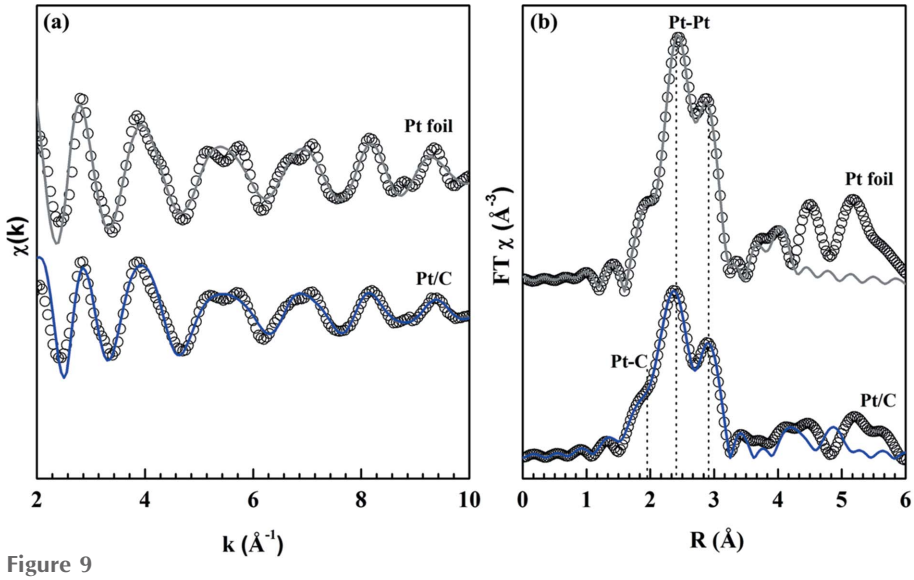

Figure 9
(a) EXAFS $\chi(k)$ signals at the Pt L_3-edge and (b) corresponding Fourier transforms for the carbon-supported Pt NPs and for a Pt^0 foil. The dots represent the experimental data and the lines indicate the best-fitted theoretical curves.

Table 1
Structural parameters obtained from EXAFS data: coordination number (N), bond distance (R) and Debye–Waller factor (σ^2) for the NPs Pt/C.

Sample	Pair	N	R (Å)	σ^2 (10^{-2} Å^2)
NPs Pt	Pt–C	0.5 ± 0.2	2.04 ± 0.02	(0.6 ± 0.1)
	Pt–Pt	10.8 ± 0.5	2.75 ± 0.03	(0.6 ± 0.1)
	Pt–Pt	1.6 ± 0.1	3.89 ± 0.03	(1.1 ± 0.4)

spond to the formation of shorter distance bonds, *i.e.* Pt–C bonds.

The quantitative results are displayed in the Table 1 for the first coordination shell. The $\mathcal{R}$-factor is a measure of the absolute deviation between the data and theory and indicates the quality of the fit. In our case, the $\mathcal{R}$-factor of 0.029 demonstrated the good agreement of theoretical and experimental curves and the reliability of the extracted structural parameters.

The reduced dimensions of the Pt particles can be inferred by the value of the first-shell coordination number, which is lower than the value for bulk Pt (12). In addition, EXAFS confirmed the lattice parameter obtained from the XRD data Rietveld refinement (a = 3.89 Å). This result corroborates the contraction on the Pt unit cell due to the reduced size of the particles.

4. Conclusions

We have presented *in situ* time-resolved DXAS measurements at the Pt L_3-edge collected during the formation of Pt NPs in aqueous solution using a specially designed dispenser–reactor system. The *in situ* study allowed us to observe this eco-friendly NPs synthesis process in real time, monitoring with great detail the local chemical environment evolution around the Pt atoms. The linear combination of each XANES spectra by an initial (Pt^{4+} ions) and final (metallic Pt) chemical states allowed us to obtain the time evolution of the zero-valent Pt fraction. As a result, it was possible to distinguish two different stages in the synthesis process: a fast nucleation event and subsequent slow growth and stabilization of NPs. It is clear that the proposed apparatus would be valuable for *in situ* monitoring of changes in the XANES/EXAFS spectra of several reactions in liquid media.

The as-prepared NPs were characterized by TEM and HRTEM, which showed that the synthesized Pt NPs were highly crystalline and quasi-spherical in shape, with a mean diameter of 4.9 nm. The Pt NPs were also supported on activated carbon, forming a Pt/C catalyst, the electronic and structural properties of which were probed by XPS, XRD and EXAFS. The results obtained confirmed that, even after being supported on activated carbon, the Pt NPs remained in the metallic chemical state and with a reduced size, as verified by XRD (reduced crystallite size) and EXAFS (reduced coordination number). The XRD and EXAFS results also gave evidence of lattice parameter contraction in the Pt NPs as compared with the bulk counterpart, as previously reported for Pt nanostructures. Future studies are planned in order to quantify the contribution of the SC to the kinetics by carrying out similar analyses with slight variations of its relative concentration.

Acknowledgements

We acknowledge the support given by FAPERGS, CNPq, CAPES, LNLS (DXAS-8150, XAFS1-14502, SXS-14437 proposals) and LNNano (TEM-HR-14037 proposal).

References

Ankudinov, A. L., Rehr, J. J. & Bare, S. R. (2000). *Chem. Phys. Lett.* **316**, 495–500.
Aricò, A. S., Shukla, A. K., Kim, H., Park, S., Min, M. & Antonucci, V. (2001). *Appl. Surf. Sci.* **172**, 33–40.
Bernardi, F., Alves, M. C. M. & Morais, J. (2010). *J. Phys. Chem. C*, **114**, 21434–21438.
Bernardi, F., Alves, M. C. M., Scheeren, C. W., Dupont, J. & Morais, J. (2007). *J. Electron Spectrosc. Relat. Phenom.* **156–158**, 186–190.
Bernardi, F., Traverse, A., Olivi, L., Alves, M. C. M. & Morais, J. (2011). *J. Phys. Chem. C*, **115**, 12243–12249.
Boita, J., Bernardi, F., Castegnaro, M. V., Nicolao, L., Alves, M. C. M. & Morais, J. (2014*a*). *J. Phys. Chem. C*, **118**, 5538–5544.
Boita, J., do Carmo Martins Alves, M. & Morais, J. (2014*b*). *J. Synchrotron Rad.* **21**, 254–258.
Boita, J., Nicolao, L., Alves, M. C. M. & Morais, J. (2014*c*). *Phys. Chem. Chem. Phys.* **16**, 17640–17647.
Boönnemann, H. & Nagabhushana, K. S. (2008). *Metal Nanoclusters in Catalysis and Materials Science*, edited by B. Corain, G. Schmid and N. Toshima, pp. 21–48. Amsterdam: Elsevier.
Bordiga, S., Groppo, E., Agostini, G., van Bokhoven, J. A. & Lamberti, C. (2013). *Chem. Rev.* **113**, 1736–1850.
Castegnaro, M. V., Kilian, A. S., Baibich, I. M., Alves, M. C. M. & Morais, J. (2013). *Langmuir*, **29**, 7125–7133.
Cezar, J. C., Souza-Neto, N. M., Piamonteze, C., Tamura, E., Garcia, F., Carvalho, E. J., Neueschwander, R. T., Ramos, A. Y., Tolentino, H. C. N., Caneiro, A., Massa, N. E., Martinez-Lope, M. J., Alonso, J. A. & Itié, J.-P. (2010). *J. Synchrotron Rad.* **17**, 93–102.
Erickson, E. M., Thorum, M. S., Vasić, R., Marinković, N. S., Frenkel, A. I., Gewirth, A. A. & Nuzzo, R. G. (2011). *J. Am. Chem. Soc.* **134**, 197–200.
Finger, L. W., Cox, D. E. & Jephcoat, A. P. (1994). *J. Appl. Cryst.* **27**, 892–900.
Frenkel, A. I. (2012). *Chem. Soc. Rev.* **41**, 8163–8178.
Frenkel, A. I., Hills, C. W. & Nuzzo, R. G. (2001). *J. Phys. Chem. B*, **105**, 12689–12703.
Girardon, J.-S., Khodakov, A. Y., Capron, M., Cristol, S., Dujardin, C., Dhainaut, F., Nikitenko, S., Meneau, F., Bras, W. & Payen, E. (2005). *J. Synchrotron Rad.* **12**, 680–684.
Guilera, G., Gorges, B., Pascarelli, S., Vitoux, H., Newton, M. A., Prestipino, C., Nagai, Y. & Hara, N. (2009). *J. Synchrotron Rad.* **16**, 628–634.
Hannemann, S., Casapu, M., Grunwaldt, J.-D., Haider, P., Trüssel, P., Baiker, A. & Welter, E. (2007). *J. Synchrotron Rad.* **14**, 345–354.
Harada, M. & Kamigaito, Y. (2011). *Langmuir*, **28**, 2415–2428.
Kim, D.-W., Lee, J.-M., Oh, C., Kim, D.-S. & Oh, S.-G. (2006). *J. Colloid Interface Sci.* **297**, 365–369.
Koningsberger, D. C. & Prins, R. (1988). *X-ray Absorption: Principles, Applications, Techniques of EXAFS, SEXAFS and XANES*, Vol. 92, edited by J. D. Winefordner and I. M. KolthoffNew York: Wiley.
Lamber, R., Wetjen, S. & Jaeger, N. I. (1995). *Phys. Rev. B*, **51**, 10968–10971.
LaMer, V. K. & Dinegar, R. H. (1950). *J. Am. Chem. Soc.* **72**, 4847–4854.

Mandal, S., Roy, D., Chaudhari, R. V. & Sastry, M. (2004). *Chem. Mater.* **16**, 3714–3724.
Moulder, J. F., Stickle, W. F., Sobol, P. E., Bomben, K. D. & Chastain, J. (1992). *Handbook of X-ray Photoelectron Spectroscopy*, p. 275. Perkin-Elmer Corporation.
Newville, M. (2001). *J. Synchrotron Rad.* **8**, 322–324.
Odzak, J. F., Argo, A. M., Lai, F. S., Gates, B. C., Pandya, K. & Feraria, L. (2001). *Rev. Sci. Instrum.* **72**, 3943–3945.
Qi, W. H. (2006). *Acta Metall. Sin.* **42**, 1065–1070.
Ramalingam, B., Mukherjee, S., Mathai, C. J., Gangopadhyay, K. & Gangopadhyay, S. (2013). *Nanotechnology*, **24**, 205602.
Ravel, B. & Newville, M. (2005). *J. Synchrotron Rad.* **12**, 537–541.
Sarma, L. S., Chen, C.-H., Kumar, S. M. S., Wang, G.-R., Yen, S.-C., Liu, D.-G., Sheu, H.-S., Yu, K.-L., Tang, M.-T., Lee, J.-F., Bock, C., Chen, K.-H. & Hwang, B.-J. (2007). *Langmuir*, **23**, 5802–5809.
Scheeren, C. W., Machado, G., Dupont, J., Fichtner, P. F. P. & Texeira, S. R. (2003). *Inorg. Chem.* **42**, 4738–4742.
Seah, M. P. & Brown, M. T. (1999). *Appl. Surf. Sci.* **144–145**, 183–187.
Sham, T. K. (1986). *J. Chem. Phys.* **84**, 7054–7055.
Steinfeldt, N. (2012). *Langmuir*, **28**, 13072–13079.
Sugimoto, T. (1987). *Adv. Colloid Interface Sci.* **28**, 65–108.
Tolentino, H., Compagnon-Cailhol, V., Vicentin, F. C. & Abbate, M. (1998). *J. Synchrotron Rad.* **5**, 539–541.
Tolentino, H. C. N., Ramos, A. Y., Alves, M. C. M., Barrea, R. A., Tamura, E., Cezar, J. C. & Watanabe, N. (2001). *J. Synchrotron Rad.* **8**, 1040–1046.
Viswanatha, R. & Sarma, D. (2007). *Nanomaterials Chemistry*, p. 170. Weinheim: Wiley–VCH Verlag GmbH.
Watanabe, N., Morais, J. & Alves, M. C. M. (2007). *J. Electron Spectrosc. Relat. Phenom.* **156–158**, 164–167.
Zabinsky, S. I., Rehr, J. J., Ankudinov, A., Albers, R. C. & Eller, M. J. (1995). *Phys. Rev. B*, **52**, 2995–3009.
Zhang, D., Okajima, T., Lu, D. & Ohsaka, T. (2013). *Langmuir*, **29**, 11931–11940.